Solar Energy 318 (2026) 115090

Contents lists available at ScienceDirect

Solar Energy

journal homepage: www.elsevier.com/locate/solener

Transparent photothermal tunnel for direct solar heating of buildings

Meher Saketh Gandharapu [a], Anudeep Katepalli [a], Anton Harfmann [b], Mathias Bonmarin [c], John Krupczak [d], Donglu Shi [a,*]

[a] The Materials Science and Engineering Program, Department of Mechanical, Materials, and Industrial Engineering, College of Engineering and Applied Science, University of Cincinnati, Cincinnati, OH, 45221, USA
[b] College of Design, Architecture, Art and Planning, University of Cincinnati, Cincinnati, OH, 45221, USA
[c] School of Engineering, Zurich University of Applied Sciences, Winterthur, 8400, Switzerland
[d] Department of Engineering, Hope College, Holland, MI, 49423, USA

ARTICLE INFO

Keywords:
Advanced building envelopes
Passive solar heating
Photothermal energy generation
Transparent solar-harvesting panels
Energy-efficient buildings
$Fe_3O_4@Cu_{2-x}S$ nanoparticles, solar tunnel

ABSTRACT

Space and water heating in buildings remain major contributors to energy demand, while many solar-based heating approaches rely on bulky collectors, active components, or complex system integration. In this work, we explore a passive heating concept based on a Photothermal Solar Tunnel (PTST), in which sunlight is guided through a sequence of transparent photothermal panels arranged in a tunnel configuration. Sunlight is collected by a rooftop solar dome and directed into the tunnel, where thin films composed of $Fe_3O_4@Cu_{2-x}S$ nanoparticles absorb ultraviolet and infrared radiation and convert it to heat while transmitting most visible light. The optical response of these films is governed by localized surface plasmon resonance, which enables selective absorption outside the visible range and allows heat generation to accumulate across multiple panels along the tunnel length. Outdoor measurements carried out under varied weather conditions, including subzero ambient temperatures, show that interior tunnel surfaces can exceed 45 °C when the ambient temperature is −6 °C, even in the absence of substantial thermal insulation. Direct solar harvesting via multiple transparent panels, enable efficient thermal energy generation resulting in a high power conversion efficiency of 60% under a sunny weather. These results suggest that the PTST can provide meaningful passive heat gain using a lightweight and modular structure. The approach avoids solar-electric conversion and large thermal storage components, offering a simple pathway for direct solar heat utilization in building envelopes.

1. Introduction

Solar energy technologies have been widely explored as potential solutions for building energy applications, particularly through photovoltaic (PV) systems [1–8]. Although PV technologies have achieved significant commercial success, their application to direct building heating remains limited by low thermal utilization efficiency and large installation footprints [9]. Conventional solar-thermal systems can provide heat more directly, but they generally rely on opaque collectors, circulating fluids, insulated storage tanks, and auxiliary heating components [1]. These systems often introduce structural complexity, increased maintenance requirements, and integration challenges in existing buildings, especially within dense urban environments.

Transparent photothermal (PT) materials provide an alternative pathway for solar-driven heating by directly converting incident sunlight into localized thermal energy while maintaining visible light transmission. In our previous work, a vertically oriented Photothermal Solar Tunnel (PTST) incorporating transparent Fe_3O_4 nanoparticle-coated panels demonstrated that localized surface plasmon resonance (LSPR) can produce substantial photothermal heating while preserving optical transparency [10]. In that system, sunlight propagated sequentially through multiple transparent PT panels arranged within a rooftop tunnel, enabling distributed thermal generation along the optical pathway.

Although rooftop-mounted configurations are effective for proof-of-concept demonstrations, practical building integration requires greater geometric flexibility. Many buildings, particularly high-rise structures, offer limited rooftop area, whereas façades and side walls provide substantially larger accessible surfaces for solar harvesting. Extending the PTST concept to façade-mounted geometries therefore represents an important step toward scalable building integration. However, changes in tunnel orientation alter the solar incidence angle, optical propagation

* Corresponding author.
E-mail address: donglu.shi@uc.edu (D. Shi).

https://doi.org/10.1016/j.solener.2026.115090
Received 30 March 2026; Received in revised form 4 August 2026; Accepted 4 September 2026

path, and heat dissipation behavior, which can significantly influence photothermal performance.

In this work, we investigate a horizontally oriented PTST designed for façade-mounted building integration (Fig. 1). The system employs transparent Fe_3O_4-based plasmonic nanoparticle coatings [10–16] that selectively absorb ultraviolet and infrared radiation while transmitting most visible light, with average visible transmittance approaching ~90% [11]. Sunlight enters laterally through a wall-mounted solar dome and propagates through a sequential multilayer arrangement of transparent PT panels, producing distributed heating without pumps, fluid circulation, or thermal storage units. By examining the influence of tunnel orientation on optical and thermal behavior, this study extends the PTST framework toward more practical building-envelope applications and provides insight into façade-integrated solar heating technologies for energy-efficient buildings.

Previous studies, including our earlier work [10], demonstrated that multilayer transparent photothermal panels can effectively harvest solar energy while maintaining optical transparency. However, those studies primarily focused on the fabrication, optical characteristics, and photothermal performance of transparent multilayer structures. The present work advances this concept in two important directions. First, a transient thermal model is developed to quantitatively describe the heating dynamics of individual transparent photothermal panels within a photothermal solar tunnel. By incorporating solar absorption together with convective and radiative heat transfer, the model provides a physics-based framework for interpreting the measured temperature evolution and predicting panel thermal behavior under outdoor solar irradiation. Second, the overall photothermal conversion efficiency of the complete tunnel system is evaluated using experimentally measured irradiance and temperature data from all six transparent photothermal panels. This system-level energy analysis establishes a quantitative engineering metric for assessing and optimizing transparent photothermal solar tunnels for passive building utility heating. Together, these developments extend transparent photothermal technology beyond material demonstration toward predictive thermal modeling and engineering design of practical building-scale solar heating systems.

2. Experimental procedure

2.1. $Fe_3O_4@Cu_{2-x}S$ nanoparticle synthesis

The $Fe_3O_4@Cu_{2-x}S$ core–shell nanoparticles used here were made following the same procedure reported in our earlier studies [17–23]. The chemistry was unchanged, so the full synthesis is described mainly for clarity. Oleylamine (60 mL) was poured into a three-neck flask and heated under nitrogen. Separately, iron acetylacetonate (700 mg) was dissolved in a mixture of oleylamine and N-methyl-2-pyrrolidone. The solution was stirred until it looked uniform and free of solids. When the oleylamine reached roughly 300 °C, the iron solution was injected quickly into the flask. The mixture was held at this temperature for about 10 min while Fe_3O_4 cores formed.

Once core formation was complete, the heating mantle was removed, and the mixture was left to cool naturally to around 70 °C. At that point, a sulfur solution, prepared by dissolving 128.28 mg of sulfur in oleylamine with a little cyclohexane to help it dissolve, was added. Immediately afterward, a copper solution containing $Cu(acac)_2$ (523.52 mg) in oleylamine and chloroform was introduced. The reaction was kept at 70 °C for another 30 min, during which the $Cu_{2-x}S$ shell gradually formed around the Fe_3O_4 cores through sequential anion and cation exchanges.

Upon completion of the shell-growth step, the reaction was allowed to cool to room temperature. The nanoparticles were collected and purified using standard washing procedures. Specifically, the product was washed three times with methanol to remove excess ligands, unreacted precursors, and low-molecular-weight byproducts. The cleaned nanoparticles were subsequently freeze-dried overnight to obtain a dry powder. For storage and further processing, the $Fe_3O_4@Cu_{2-x}S$ nanoparticles were redispersed in toluene.

The photothermal coating was prepared by dispersing Fe_3O_4 nanoparticles into a two-part transparent epoxy system consisting of resin and hardener mixed according to the manufacturer's specifications [11–16]. Prior to curing, the nanoparticles were mechanically mixed into the epoxy matrix to achieve uniform dispersion. Because the

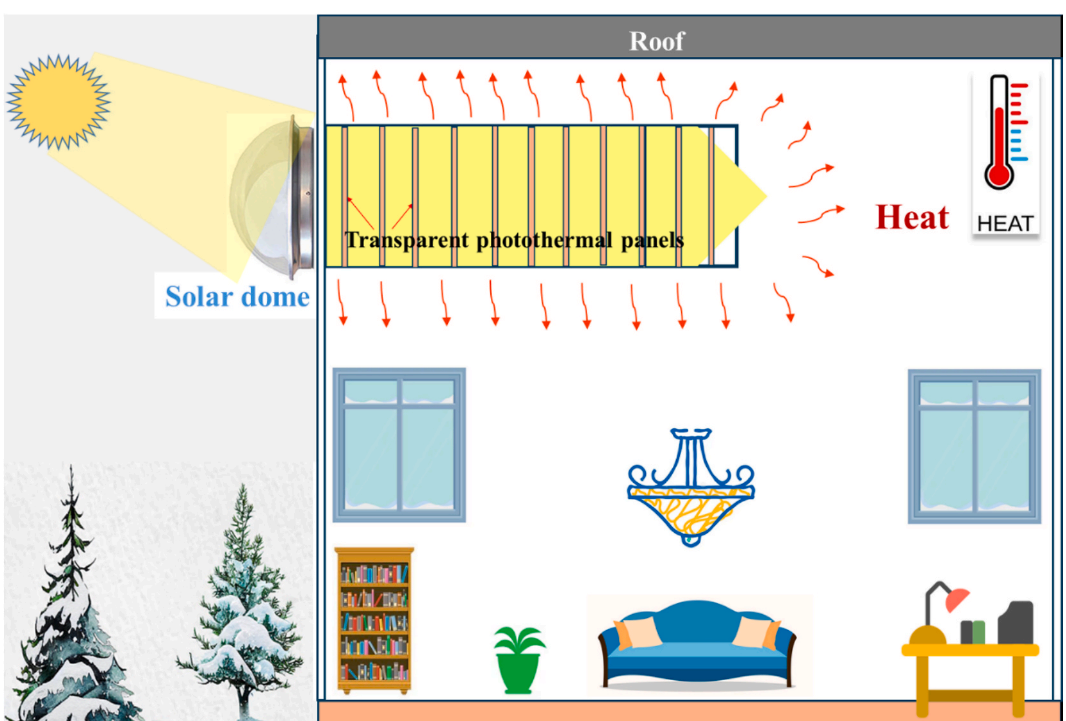

Fig. 1. Schematic diagram showing the concept of the utility heating with the Photothermal Solar Tunnel (PTST) and the photothermal (PT) panels.

nanoparticles were synthesized with surface-bound organic ligands and maintained at relatively low loading concentrations, no additional solvent was required during coating preparation, and no visible particle agglomeration was observed in the cured films.

The Fe_3O_4@$Cu_{2-x}S$ nanoparticles possess a well-established core–-shell architecture previously verified through TEM, HRTEM, EDS mapping, and XRD analyses reported in our earlier studies [10–14]. Beyond structural stabilization, the core–shell geometry facilitates plasmonic hybridization between the Fe_3O_4 core and $Cu_{2-x}S$ shell. Such hybridization modifies the local electromagnetic field distribution and broadens the spectral absorption bandwidth through mode coupling and plasmon splitting effects, thereby enhancing overall solar harvesting and photothermal energy conversion.

2.2. Photothermal panel design

The photothermal (PT) panels were made by coating flat glass plates with a polymer layer containing dispersed nanoparticles. The dimensions of the glass substrates are 230 mm × 230 mm with a thickness of 2.38 mm. For the coating, Fe_3O_4@$Cu_{2-x}S$ nanoparticles were mixed directly into an epoxy resin. The nanoparticle concentration in the polymer was set to 1 mg per cubic centimeter of resin. The epoxy–nanoparticle mixture was stirred for approximately 10 min. This step was done to distribute the nanoparticles as evenly as possible and to reduce the presence of visible air bubbles in the solution. After mixing, 50 mL of the polymer solution was used for each glass substrate. The solution was spread across the glass surface using a doctor blade, following the same approach described in Ref. [10]. This method allowed the coating to be applied over the full area of the panel with reasonably uniform thickness. Once coated, the glass panels were left undisturbed at room temperature for 24 h. During this time, the epoxy cured and formed a solid photothermal layer on the glass surface. After curing, the panels were examined visually to confirm that the coating was continuous and free of obvious defects before they were used in the solar tunnel experiments.

2.3. Engineering of photothermal solar tunnel

The Photothermal Solar Tunnel (PTST) was constructed as depicted in Fig. 2. Fig. 2a shows a photograph of the solar tunnel integrated with a commercial solar dome (Sun Tek), which was used for solar harvesting and light transmission through the tunnel. The exterior surface of the dome was insulated with a thin polyethylene (PE) sheet to minimize thermal losses. The interior surface of the solar tunnel was lined with a thin aluminum sheet serving as a reflective layer to enhance sunlight transmission and improve light distribution throughout the tunnel.

As shown in Fig. 2b, the solar dome was connected to a cylindrical tunnel with a diameter of 35.56 cm and a length of 106 cm. Six transparent photothermal (PT) panels were sequentially arranged in parallel within the tunnel with a uniform spacing of 5 cm between adjacent panels. The first PT panel was positioned 5 cm below the base of the solar dome. This multilayer arrangement was designed to enable progressive spectral harvesting and distributed thermal generation along the optical pathway while maintaining partial visible light transmission through successive panels.

As illustrated in Fig. 2b, one K-type thermocouple (red arrow) was attached to the center surface of each PT panel to monitor panel temperature, while four additional thermocouples (yellow arrows) were positioned near the bottom region of the solar dome to monitor local temperature distribution. The locations and distances of these thermocouples are indicated in Fig. 2b. Repeated outdoor photothermal measurements conducted under comparable solar irradiation conditions showed consistent thermal response trends throughout the PTST system. Temperature measurements were obtained using calibrated K-type thermocouples with experimental uncertainty primarily arising from ambient environmental fluctuations and solar irradiance variability during outdoor operation. The observed thermal behavior remained reproducible across repeated measurements, confirming the stability of the distributed photothermal heating mechanism.

The temperatures from all K-type thermocouples were continuously recorded using a computerized data acquisition system and stored electronically for subsequent analysis. Automated data logging eliminated manual recording errors and ensured consistent monitoring throughout the outdoor testing period.

2.4. Experimental procedure

The experiments were carried out outdoors on the campus of University of Cincinnati in October and November of 2025 and in January of 2026. These dates correspond to fall and winter seasons in Cincinnati, Ohio, when the sun follows a relatively low trajectory and the duration of direct illumination is limited. Fig. 3 schematically depicts the sun's daily trajectory from sunrise to sunset on the dates when the experiments were conducted. An inset in the diagram indicates the daily path of the sun during these periods from a three-dimension perspective. As shown in this diagram, the solar tunnel attached with a solar dome is placed horizontally on the ground for solar harvesting on the side wall of the building (see Fig. 1). A hemispherical solar dome is fixed at the entrance of the tunnel and used to collect incoming sunlight. During the experiments, as the sun moved across the sky, sunlight entered the dome at different angles and propagated into the solar tunnel (Figs. 1 and 2). As sunlight passed through six parallel photothermal panels, it was directly converted into photothermal energy, raising the temperature inside the solar tunnel. Temperature data were collected continuously as

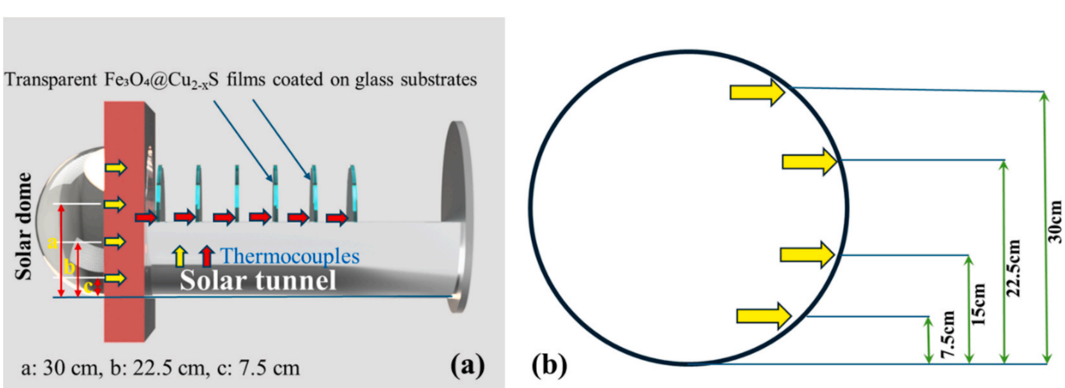

Fig. 2. (a) Schematic diagram showing Photothermal Solar Tunnel (PTST) with a solar dome. Six red arrows indicate the thermocouples located at the center of the panels with 5 cm spacing between adjacent panels. (b) The top view of the solar dome with four yellow arrows indicating the positions of the thermocouples inside. (For interpretation of the references to colour in this figure legend, the reader is referred to the web version of this article.)

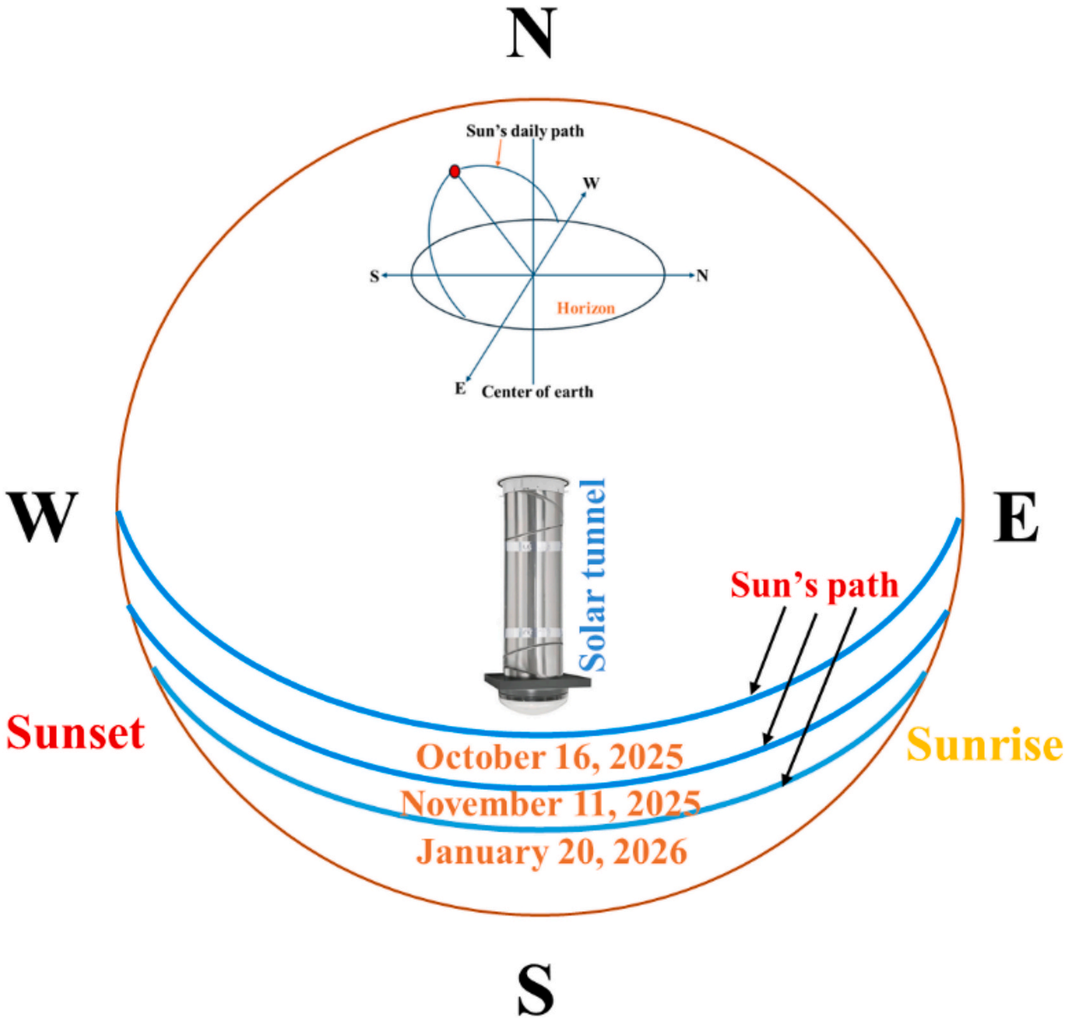

Fig. 3. Schematic diagram illustrating the daily path of the sun from sunrise to sunset experrelative to the solar tunnel and hemispherical solar dome. The sun's trajectory is shown for the experimental periods, indicating the changing solar elevation and incidence angle throughout the day. The solar tunnel is positioned horizontally on the ground, with the solar dome mounted at the tunnel entrance to collect incoming sunlight as the sun moves across the sky. The diagram is intended to provide geometric context for the photothermal measurements rather than represent a specific time scale. The inset provides the 3D perspective of the sun's daily path.

the sun progressed along its daily path. The measured heating curves therefore reflect the changing solar elevation and incidence angle over the course of the day, rather than a fixed illumination condition. Consequently, the measured heating behavior reflects realistic solar-to-thermal conversion under natural outdoor conditions, in contrast to experiments performed under simulated solar irradiation with constant light power density. Under real sunlight, the incident light intensity varies continuously throughout the day and is further influenced by transient cloud cover, leading to more practical and representative performance evaluation.

3. Results

3.1. Characterization of the Fe_3O_4@$Cu_{2\text{-}x}S$ nanoparticles and thin films

The synthesis and characterization of Fe_3O_4@$Cu_{2-x}S$ nanoparticles and thin films have been previously reported [10,11,23–25]. Fig. 4 presents the characterization results of the transparent Fe_3O_4@$Cu_{2\text{-}x}S$ thin films. The transmission electron microscopy (TEM) image in Fig. 4a shows monodispersed nanoparticles with an average diameter of 15 nm. Fig. 4b shows the photograph of the spin-coated glass substrate with the Fe_3O_4@$Cu_{2\text{-}x}S$ nanoparticles indicating significant transparency which is essential for the multiple panel application in the solar tunnel [10]. A typical Fe_3O_4@$Cu_{2\text{-}x}S$ panel exhibits an average visible transmittance (AVT) of 65% at a concentration of 9.45×10^{-5} g/cm^2 measured using LS116 light transmittance meter. This AVT ensures efficient solar light transmission through the solar tunnel for generating significant thermal energy for building utility heating. Fig. 4c the absorption spectrum of Fe_3O_4@$Cu_{2\text{-}x}S$ solution. As can be seen in this figure, Fe_3O_4@$Cu_{2\text{-}x}S$ has a strong absorption in both UV and IR regions whiling exhibiting a valley in the visible band showing the typical "U" shaped behavior rendering the thin film transparent. This IR absorption is particularly important for photothermal heating based on the Localized Surface Plasmon Resonance (LSPR) [13,14]. With the "U"-shaped optical absorption behavior, it is possible to achieve high transparency through multiple panels while covering both UV and IR photos to thermal energy via LSPR. Since the Fe_3O_4@$Cu_{2\text{-}x}S$ film is extremely thin on the order of 500 nm [14], its IR absorption is not observed as shown in Fig. 4d. However, these thin films are cable of converting solar light to thermal energy efficiently under direct natural solar irradiation as will be shown in the photothermal experiments.

The optical transmittance and absorbance spectra of the transparent photothermal panels were measured using a UV–Vis-NIR spectrophotometer without an integrating sphere accessory. Therefore, the measured transmittance primarily represents the direct transmitted optical component and does not fully account for diffusely scattered

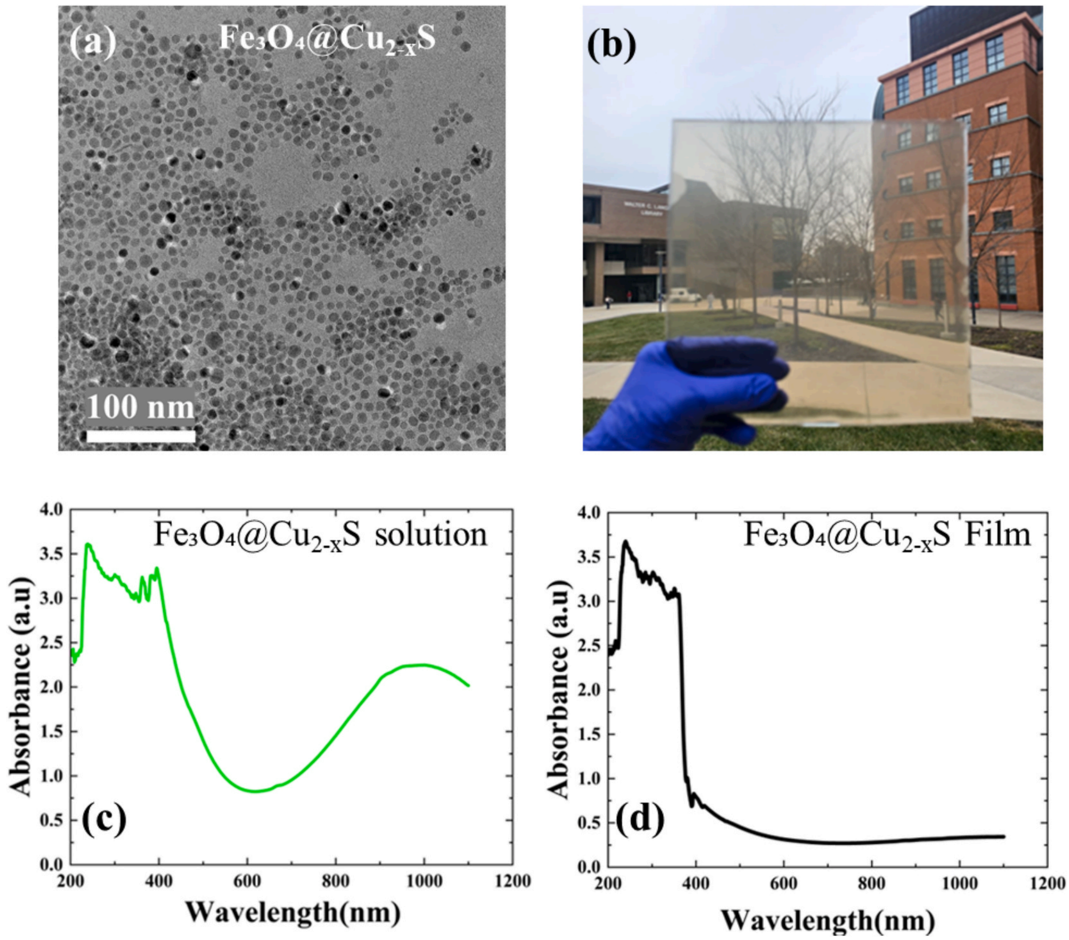

Fig. 4. (a) TEM image $Fe_3O_4@Cu_{2-x}S$ nanoparticles, (b) photograph of the $Fe_3O_4@Cu_{2-x}S$ thin film on glass substrate with AVT of 65%, (c) optical absorption spectrum of the $Fe_3O_4@Cu_{2-x}S$ solution () showing the "U"- shaped characteristic, and (d) optical absorption spectrum of the $Fe_3O_4@Cu_{2-x}S$ thin film on glass substrate.

photons or angular-dependent transmission. This limitation may lead to a slight underestimation of the total hemispherical optical transmission of the photothermal panels. However, the measured direct transmission is suitable for evaluating the spectral attenuation behavior of the panels within the photothermal solar tunnel, where transmitted solar radiation is guided along the tunnel axis toward subsequent photothermal layers. Future studies incorporating integrating-sphere measurements will provide additional information regarding diffuse transmission, scattering losses, and complete optical energy balance of the system.

The numerical values reported in this section were obtained directly from experimental characterization and outdoor photothermal measurements. The nanoparticle diameter was determined from TEM image analysis, while the optical transmittance and absorption spectra were measured using UV–Vis-NIR spectroscopy. The thin-film thickness (~500 nm) was experimentally measured as previously reported in Ref. [14]. Thermal data presented throughout the photothermal experiments were recorded using calibrated K-type thermocouples positioned at designated locations within the photothermal solar tunnel under natural solar irradiation conditions.

3.2. Photothermal experiments

The photothermal experiments under natural sunlight were conducted through October of 2025 to January of 2026. Some experimental dates are indicated in Fig. 3 with the depictions of the daily sun's path. In these experiments, the Photothermal Solar Tunnel (PTST) with a solar dome was positioned horizontally on the ground facing south on the main campus of University of Cincinnati (Fig. 3). Fig. 5a shows the experimental set up of PTST on October 16, 2025, with the south facing solar dome for harvesting and transmitting sunlight through the solar tunnel in order to generate thermal energy on the six PT panels [10]. Fig. 5b shows the heating curves with the thermocouples located on the top of each PT panel as depicted in Fig. 3b. The experiment started at 10:00 AM and finished at 5:30 PM and the ambient temperature varied between 15 ℃ to 25 ℃ during the experiment. As can be seen in this figure, the temperatures at these thermocouple positions on the six panels are initially around 25 ℃ and begin to rise rapidly due to the photothermal effect of the $Fe_3O_4@Cu_{2-x}S$ nanoparticles, and reach the peaks at the noon time (~ 142 min). This is consistent with the sun path as depicted in Fig. 3 where sunlight is irradiating directly on the top of solar dome. However, due to attenuation of the sunlight through the multiple PT panels, the peak temperature decreases from the maximums near 66.4 ℃ to 53 ℃. After the sun passes through the noon time, the temperatures experience graduate decrease and down to 29 ℃ at 5:30 PM just before sunset.

As depicted in Fig. 2b, there are four thermocouples located inside the solar dome and hearting curves registered from them are plotted in Fig. 5c. As can be seen in this figure, the temperature variations are similar to those shown in Fig. 5b but consistently fall within each other indicating uniform temperature distributions in the solar dome. In addition, the ambient temperature distribution is also shown in this figure for comparison. The sharp contrasts between them indicate the strong photothermal effect of the $Fe_3O_4@Cu_{2-x}S$ nanoparticles and the heating efficiencies.

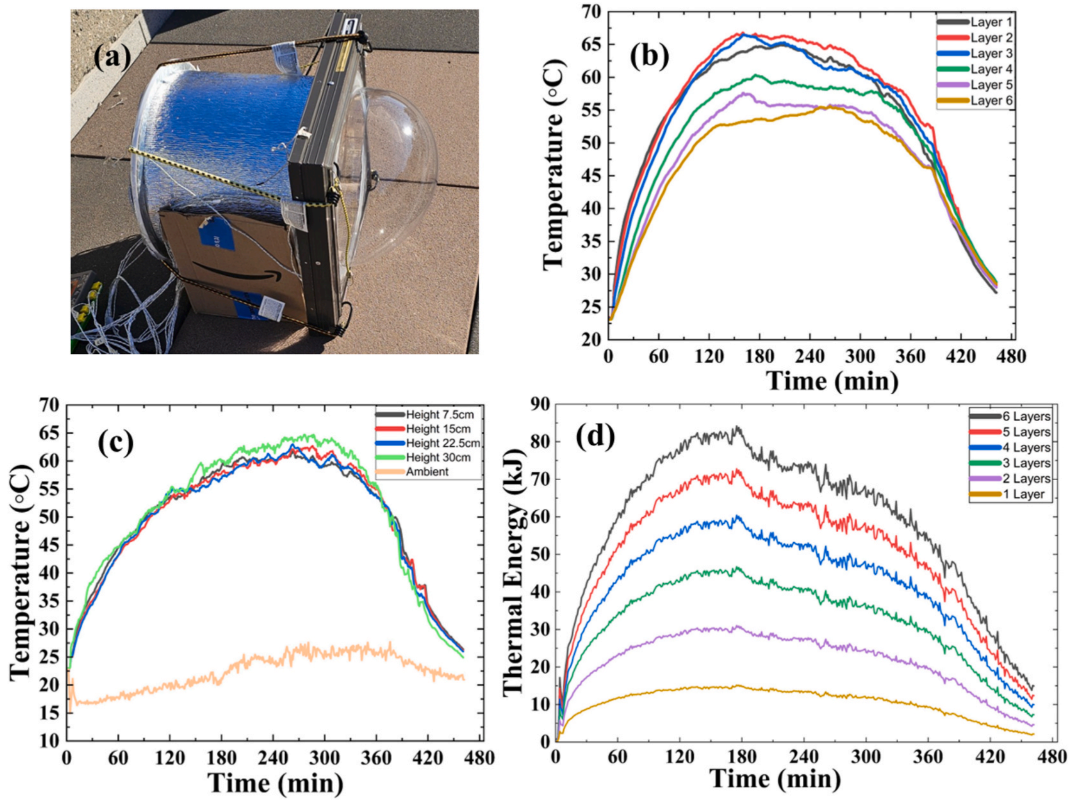

Fig. 5. (a) South-facing Photothermal Solar Tunnel (PTST) on the main campus of University of Cincinnati for solar harvesting experiments. The experiments were conducted on October 16th, 2025, from 10:00AM to 5:30PM with an ambient temperature varying between 15 and 25 ∘C; (b) Temperature vs time heating curves obtained from the thermocouples located on each photothermal panels; (c) Temperature vs time heating curves obtained from the four thermocouples in the solar dome as shown in Fig. 2b, and (d) Thermal energy vs time calculated from the heating curves shown in Fig. 5b.

Using the heating curves from Fig. 5b, the thermal energy generated can be calculated according to

$$Q = \Delta T_{max} \times m \times Cp.$$

where ΔT_{max} is the maximum temperature rise obtained from the heating curve, m is the combined mass of the glass substrate and polymer substrate, Cp is the effective specific heat capacity of the panel, and ΔT is the measured temperature increase. The mass of the $Fe_3O_4@Cu_{2-x}S$ nanoparticles was neglected because it is negligible compared with the masses of the supporting substrates. Therefore, the effective thermal capacity of the panel was determined from the combined contributions of the glass and polymer substrates ($mCp = m_1C_1 + m_2C_2$), and this combined thermal capacity was used in the thermal energy calculations [14]. Using this equation, the thermal energies are calculated and plotted as shown in Fig. 5d. As shown in this figure, for a single panel, approximately 14000 J of thermal energy is produced over 120 min of heating. As the number of panels increases, the total thermal energy output scales accordingly, reaching up to 77,000 J when six panels are utilized. This proportional increase indicates the scalability of the PTST system in thermal energy generation and its potential for enhanced performance with the integration of additional panels.

When solar radiation passes through the solar tunnel, some absorption and heat generation within the tunnel itself will occur even with the highly reflective tunnel walls. Using data on the measured solar radiation intensity of 52 mW/cm^2 at the tunnel entrance, and a reflectivity of 97% for the reflective aluminum coating of the tunnel walls, a total of 16 kJ of heat will be generated in 120 min by the 1.164 m^2 of reflective coating on the tunnel walls. This is comparable to the heat generated by one of the panels. While the heat generated in the reflective tunnel wall is appreciable enough to merit consideration, it is overall a minor contribution compared to the effect of the panels. Additionally, the tunnel wall has 22 times the surface area of a panel, highlighting the ability of the panels as the dominant heat generation source. The small amount of unavoidable self-heating of the reflective tunnel walls add a small amount of additional heating to the primary heating source of the photothermal panels.

In order to determine the solar harvesting and thermal energy generation efficiencies of the PTST under cloudy conditions, an experiment was carried out on November 11th, 2025, from 10:30 AM to 5:30 PM with an ambient temperature varying between 2 °C and 5 °C (Fig. 6). It must be noted that the weather condition was significantly different from that of October 16, 2025, not only with much lower ambient temperature, but also predominantly overcast or cloudy, not a clear, sunny day.

As shown in Fig. 6, the weather conditions have strong effects on the photothermal energy generation. As shown in Fig. 6a, the south-facing PTST is positioned on the ground with remaining snow from the previous day indicating the typical winter condition in Cincinnati, Ohio. However, even under cold and cloudy conditions, the PTST reached the highest temperature of 34 °C. Note that the initial temperature is at 25 °C since the system was set up inside the laboratory first before taking it to the open-air campus. Interestingly, the heating curves exhibit two peaks at the moments of sunny sky while the two valleys correspond to cloud cover in the sky blocking the sun, therefore reducing the photothermal effect of the PT panels. Consistently, the four thermocouples within the solar dome show similar trends under the cloudy conditions. In the same way, the thermal energies are calculated with the heating curves shown in Fig. 6b and plotted as function of time as shown in Fig. 6d [14].

To further demonstrate solar harvesting capabilities of PTST, another experiment was conducted on January 20th, 2026, from 9:30 AM to 5:00

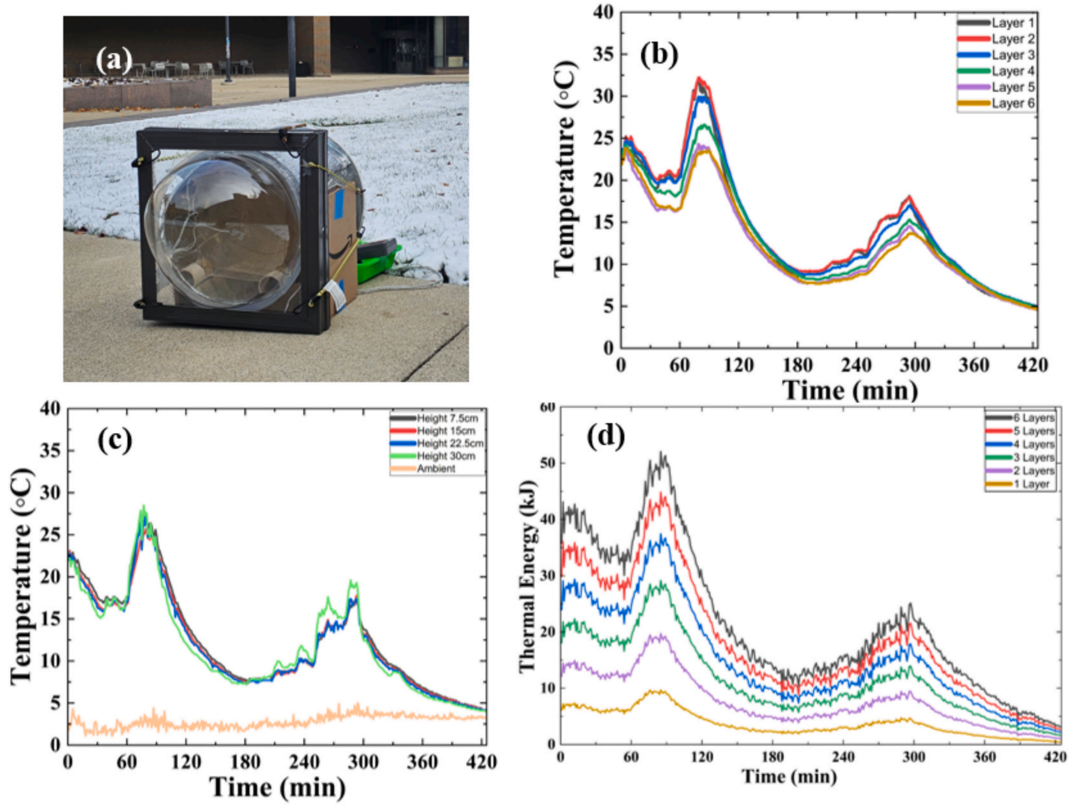

Fig. 6. a) South-facing Photothermal Solar Tunnel (PTST) on the main campus of University of Cincinnati for solar harvesting experiments. The experiments were conducted on November 11th, 2025 from 10:30AM to 5:30PM with an ambient temperature varying between 2 °C and 5 °C; (b) Temperature vs time heating curves obtained from the thermocouples located on each photothermal panels; (c) Temperature vs time heating curves obtained from the four thermocouples in the solar dome as shown in Fig. 2b, and (d) Thermal energy vs time calculated from the heating curves shown in Fig. 6b.

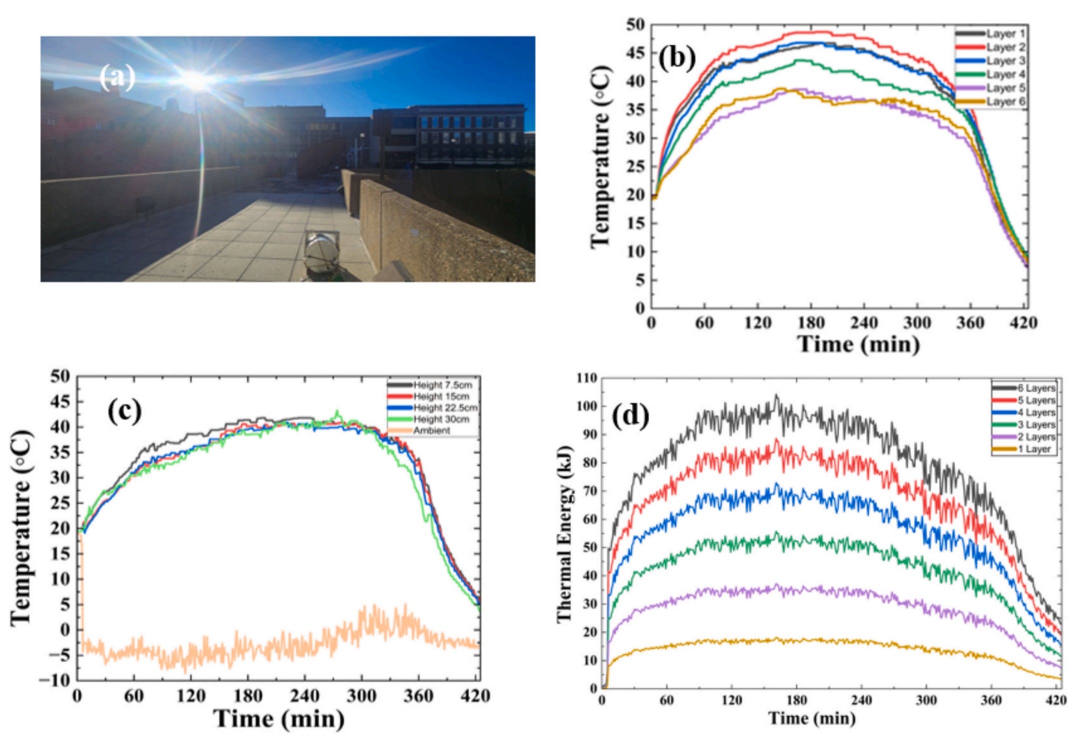

Fig. 7. a) South-facing Photothermal Solar Tunnel (PTST) on the main campus of University of Cincinnati for solar harvesting experiments. The experiments were conducted on January 20th, 2026 from 9:30 AM to 5:00 PM with an ambient temperature varying between −6 °C to −2 °C; (b) Temperature vs time heating curves obtained from the thermocouples located on each photothermal panels; (c) Temperature vs time heating curves obtained from the four thermocouples in the solar dome as shown in Fig. 2b, and (d) Thermal energy vs time calculated from the heating curves shown in Fig. 6b.

PM with an ambient temperature varying between −6 °C to −2 °C. Although the temperature was extremely low on that day, the weather was completely sunny throughout the day. Fig. 7a shows the sunny weather with a south-facing PTST on the campus of the University of Cincinnati. As shown in Fig. 7b, even under extremely low ambient temperature between −6 °C to −2 °C, the PTST exhibits significant temperature increases peaking in the range between 48.7 °C and 38.5 °C for the six thermocouples on the PT panels. Note that the system was set up inside the laboratory first resulting in the initial temperature around 20 °C. At sunset around 5 PM, the temperatures drop to range between 6 °C and 8 °C. It should be particularly noted that, due to high transparency of the PT panels, even those at the far end of the solar tunnel still produced sufficient thermal energy responsible for raising temperature in the range of 35 °C near the noon time. The heating curves taken from the four thermocouples inside the solar dome (Fig. 2b) are consistent with those from Fig. 7b. The reference ambient temperature was also shown in this figure in the sub-zero range showing pronounced photothermal heating of the PTST. The photothermal energies generated on different panels are calculated with the heating curve data from Fig. 7b and plotted in Fig. 7c [14].

4. Discussion

Coating the Fe_3O_4 cores with a $Cu_{2-x}S$ shell introduces a strongly correlated plasmonic semiconductor whose optical response is governed by a degenerate hole plasma arising from copper vacancy defects [26,27]. In the heavily doped limit, the carrier distribution approaches a Fermi–Dirac gas, and the dielectric response can be derived from the linear-response formalism. Within the random phase approximation (RPA), the longitudinal dielectric function takes the form [28–30]

$$\varepsilon(\mathbf{q},\omega) = 1 - \frac{e^2}{\varepsilon_0 q^2}\Pi(\mathbf{q},\omega), \tag{1}$$

where $\Pi(\mathbf{q},\omega)$ is the polarization function of the interacting hole gas. In the long-wavelength limit $q\rightarrow 0$, this reduces to a Drude-like response with corrections due to band nonparabolicity and interband coupling, yielding [28–30]

$$\varepsilon(\omega) = \varepsilon_\infty - \frac{\omega_p^2}{\omega(\omega + i\gamma)} + \Delta\varepsilon_{\text{inter}}(\omega), \tag{2}$$

where $\gamma \sim 1/\tau$ encodes carrier scattering processes (phonon, impurity, and defect assisted), and $\Delta\varepsilon_{\text{inter}}$ captures higher-energy transitions that renormalize the background permittivity.

A more refined expression for the plasma frequency in a nonparabolic valence band is

$$\omega_p^2 = \frac{e^2}{\varepsilon_0}\int \frac{d^3k}{(2\pi)^3}\left(-\frac{\partial f(E_k)}{\partial E_k}\right)v_k^2, \tag{3}$$

where $v_k = \nabla_k E_k/\hbar$ is the group velocity. This highlights that ω_p is not simply density-driven but also depends sensitively on band curvature, which is strongly modified in copper-deficient chalcogenides.

Plasmonic resonance and energy dissipation

The quasi-static polarizability [28–30]

$$\alpha(\omega) = 4\pi a^3 \frac{\varepsilon(\omega) - \varepsilon_m}{\varepsilon(\omega) + 2\varepsilon_m} \tag{4}$$

emerges as the leading-order term in a multipole expansion of the full Mie solution. However, a more complete treatment includes radiative damping and dynamic depolarization, leading to a corrected polarizability:

$$\alpha_{\text{eff}}(\omega) = \frac{\alpha(\omega)}{1 - \frac{ik^3}{6\pi}\alpha(\omega) - \frac{k^2}{a}\alpha(\omega)}, \tag{5}$$

where the k^3 term represents radiation reaction and the k^2 term captures phase retardation. These corrections become non-negligible as particle size increases toward the skin depth.

The resonance condition generalizes from the Fröhlich criterion to a complex root of the denominator:

$$\text{Re}[\varepsilon(\omega_r)] = -2\varepsilon_m \text{and} \text{Im}[\varepsilon(\omega_r)] \ll |\text{Re}[\varepsilon(\omega_r)]|, \tag{6}$$

ensuring a high quality factor

$$Q = \frac{\omega_r}{2\gamma_{\text{eff}}}. \tag{7}$$

For $Cu_{2-x}S$, γ_{eff} is significantly larger than in noble metals due to strong defect scattering, leading to broader but tunable resonances in the infrared.

Core–Shell hybridization and mode splitting

For the $Fe_3O_4@Cu_{2-x}S$ architecture, the plasmonic response is more accurately described as a hybridized mode resulting from the coupling of inner and outer surface charge oscillations. Using plasmon hybridization theory, the system supports bonding and antibonding modes with energies approximately given by [28–30]

$$\omega_\pm^2 \approx \omega_s^2\left(\frac{(1+2\eta) \pm \sqrt{(1+2\eta)^2 - 8\eta(1-\beta)}}{2(1-\beta)}\right), \tag{8}$$

where $\eta = (\varepsilon_c - \varepsilon_s)/(\varepsilon_c + 2\varepsilon_s)$ and $\beta = (a_c/a_s)^3$. These modes arise from the interaction between polarization charges at the core–shell and shell–environment interfaces, leading to spectral splitting and enhanced field localization within the shell.

Near-field enhancement and energy conversion

The local electric field enhancement near the plasmon resonance can be expressed as [28–30]

$$\frac{|\mathbf{E}_{\text{loc}}|^2}{|\mathbf{E}_0|^2} \sim \left|\frac{3\varepsilon_m}{\varepsilon(\omega) + 2\varepsilon_m}\right|^2, \tag{9}$$

which can exceed orders of magnitude near resonance. The absorbed electromagnetic energy is dissipated via Joule heating:

$$P_{\text{abs}} = \frac{\omega}{2}\varepsilon_0 \int_V \varepsilon_2(\omega)\left|\mathbf{E}(\mathbf{r},\omega)\right|^2 dV, \tag{10}$$

linking plasmon excitation directly to photothermal conversion. In $Fe_3O_4@Cu_{2-x}S$, this absorbed energy can further couple into manganic or lattice degrees of freedom in the magnetic core, opening pathways for magneto-thermal or spin-dependent processes.

The $Cu_{2-x}S$ shell operates in a regime where defect-induced carrier degeneracy gives rise to a tunable infrared plasmon, whose resonance condition is governed by a balance between collective oscillation (ω_p), damping (γ), and dielectric screening. The core–shell geometry introduces additional degrees of freedom through electromagnetic coupling and mode hybridization; significantly amplifying absorption and local field intensity compared to bare Fe_3O_4. This multiscale interplay—spanning band structure, many-body response, and electromagnetic boundary conditions—underpins the enhanced infrared functionality of the composite system.

Most photothermal materials reported for solar energy conversion and thermal management rely on three-dimensional, optically opaque architectures designed to maximize broadband absorption. Common examples include carbon-based absorbers, carbon nanotube forests, graphene foams, black polymers, and metal–carbon composites, all of which intentionally suppress optical transmission in order to achieve strong light-to-heat conversion [31–34]. While these bulk and dark materials are highly effective absorbers, their intrinsic opacity restricts their use to single-surface or single-layer configurations, limiting scalability in systems where light must propagate through extended geometries. As a result, such approaches are not well suited for applications that require both solar harvesting and optical transparency.

In contrast to all previous research, using thin, optically transparent films arranged in a multi-panel Photothermal Solar Tunnel (PTST) enables both transmission of light and photothermal energy generation. Sunlight entering the tunnel transmits most of the visible component, while successive panels coated with $Fe_3O_4@Cu_{2-x}S$ progressively absorb infrared photons. Each panel captures only part of the infrared energy, but the tunnel confines the light and reduces convective losses, producing a cumulative temperature rise that would be impossible with a single coated surface or with Fe_3O_4 alone. Putting these observations together, it's clear why the $Cu_{2-x}S$ shell is essential for the PTST. The shell absorbs infrared light efficiently, capturing the part of sunlight that efficiently produces heat, while the Fe_3O_4 core and transparent panel layout let energy accumulate as light travels down the tunnel. This combination produces strong, repeatable heating across different seasons.

In our measurements, the $Fe_3O_4@Cu_{2-x}S$ coatings consistently converted sunlight into heat, even when the ambient temperature and solar intensity varied considerably. The performance is tied closely to the coatings' optical properties: strong absorption in the ultraviolet and infrared allows efficient heat generation, while the visible range remains largely transparent. Sunlight spans a broad spectrum, from ultraviolet through visible light into infrared. Ideally, a solar absorber should capture as much of the non-visible spectrum as possible while letting visible light through. The absorption spectrum of the $Fe_3O_4@Cu_{2-x}S$ coatings (Fig. 8) shows that films absorb strongly in the near-UV and across a wide infrared band, while visible light passes through, producing a U-shaped profile. For comparison, the dashed line in Fig. 8 shows an idealized response, with maximum absorption in UV and IR and minimal absorption in visible wavelengths. High visible transmittance allows sunlight to reach successive panels, while UV and infrared are absorbed at each stage, generating heat along the tunnel. In practice, this makes the tunnel act like a transparent heat radiator. Minor variations between panels were observed, but the overall effect is robust, making this approach suitable for warming large building areas without blocking light [10–16].

Thermal simulation

A photothermal solar tunnel (PTST) system was operated on 16 October 2025 from 10:00 to 17:30 under clear-sky conditions (Fig. 5).

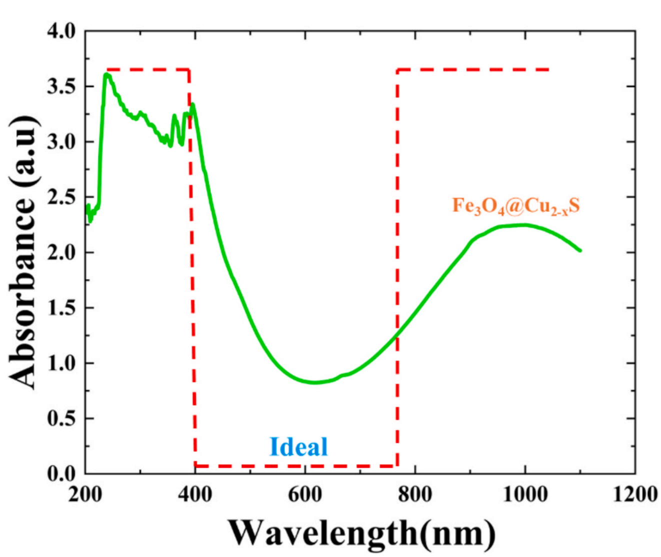

Fig. 8. Optical absorption of $Fe_3O_4@Cu_{2-x}S$ nanoparticles with the characteristic of the U-shaped behavior, i.e. strong UV and IR absorptions with minimum in the visible band enabling the multiple transparent panel application in PTST. The dash line represents the ideal behavior with the maximum UV/IR and minimum visible absorptions.

Solar radiation was collected by a south–facing dome and redirected into a horizontal cylindrical tunnel (inner diameter 35.56 cm, length 106 cm) positioned on the ground. Inside the tunnel, six transparent photothermal (PT) panels – each incorporating $Fe_3O_4@Cu_{2-x}S$ nanoparticles – were installed in a parallel arrangement. The first panel was located 5 cm below the base of the solar dome, and the remaining panels were placed at uniform 5 cm center–to–center spacing. Each PT panel exhibited an average visible transmittance (AVT) of ~ 65%, resulting in progressive attenuation of the optical flux along the tunnel length.

To interpret the measured temperature–time profiles, a lumped thermal energy balance was formulated for each panel. For panel i, the governing equation is:

$$m_i c_{p,i}\frac{dT_i}{dt} = \alpha_i A_i I_i(t) - \left[h_i A_i (T_i - T_{\text{amb}}(t)) + \varepsilon_i \sigma A_i \left(T_i^4 - T_{\text{amb}}^4\right)\right]. \quad (11)$$

here:

- $m_i c_{p,i}$ = effective thermal mass of panel i (substrate + nanoparticle layer)
- α_i = spectral absorptance under transmitted solar flux
- A_i = illuminated area
- $I_i(t)$ = incident optical power density
- h_i = effective convective heat-transfer coefficient inside the tunnel
- ε_i = effective emissivity
- σ = Stefan–Boltzmann constant
- $T_{\text{amb}}(t)$ = ambient air temperature

The radiative emission term was retained because panel temperatures rose well above ambient during peak solar input.

Panel dimensions

- 23 cm × 23 cm
- Area:

$A = 23 \times 23 = 529\text{cm}^2$

Glass thickness

- t = 2.38 mm = 0.238 cm

Glass density

- Typical soda–lime glass:

$\rho \approx 2.50\ \text{g/cm}^3$

Panel volume

$V = A \times t = 529\ \text{cm}^2 \times 0.238\ \text{cm} = 125.9\ \text{cm}^3$

Panel mass

$m = \rho V = 2.50\ \text{g/cm}^3 \times 125.9\ \text{cm}^3 = 314.7\ \text{g}$

Specific heat of glass

$c_p = 0.84\ \text{J g}^{-1}\ \text{K}^{-1}$

Thermal capacity of one panel

Given:

- Panel mass: m = 314.7 g
- Glass specific heat: c_p = 0.84 J g^{-1} K^{-1}

$mc_p = 314.7 \times 0.84\ \text{Jg}^{-1}\ \text{K}^{-1} = 264.35\ \text{J K}^{-1}$

The lumped–capacitance assumption is appropriate for the PT panels. Using a glass thermal conductivity

$k \approx 1\ \text{Wm}^{-1}\text{K}^{-1}$,

a convective heat–transfer coefficient.

$h \approx$ 20-25 $\mathrm{W\,m^{-2}\,K^{-1}}$, and a characteristic length

$$L_c = t/2 = 1.19 \times 10^{-3}\ \mathrm{m}$$

for the 2.38 mm–thick panel, the Biot number is

$$\mathrm{Bi} = \frac{hL_c}{k} \approx 0.03 \lll 0.1,$$

which confirms that internal temperature gradients within the panel are negligible.

Panel area:

$$A = 529\ \mathrm{cm}^2$$

$$(mc_p)'' = \frac{264.35\ \mathrm{J\ K^{-1}}}{529\ \mathrm{cm}^2} = 0.499\ \mathrm{J\ cm^{-2}\ K^{-1}}$$

Value used in PCE calculations

$$(mc_p)'' = 0.50\ \mathrm{J\ cm^{-2}\,K^{-1}}$$

Optical attenuation along the tunnel was incorporated through a simple multiplicative transmission model:

$$I_i(t) = I_1(t)\,\eta^{i-1}, \tag{12}$$

where:

- $I_1(t)$ is the irradiance incident on the first panel (52 $\mathrm{mW\ cm^{-2}}$),
- η is the per–panel transmission factor, consistent with the measured AVT and estimated *tobe*0.72.

At this stage of modeling, it is physically reasonable to assume:

- identical h_i for all panels,
- identical α_i,
- and a slowly varying or piecewise–constant $I_1(t)$ over the course of the day.

The measured temperature trajectories serve two critical functions:

1. Model validation:
2. Assess whether the lumped-parameter formulation adequately reproduces the observed heating and cooling behavior of each panel.
3. Parameter identification:
4. Constrain unknown thermal parameters – such as h, αI_1, or effective per-panel transmission – through inverse fitting of the simulation to experimental data.

This inverse problem is difficult to address using point-and-click curve-fitting tools (e.g., Prism), but is readily solved in a computational scripting environment through numerical ODE integration and nonlinear optimization.

Fig. 9 presents the experimentally measured surface temperature of Panel 1 together with the corresponding heating–cooling simulation generated using a lumped-parameter thermal model. The panel undergoes rapid heating during the initial portion of the experiment, reaching a peak temperature of approximately 65 °C, and subsequently cools gradually as the incident solar flux diminishes later in the day. To reproduce this behavior, the simulation applies a first-order energy balance that incorporates an effective absorbed-power function $a(t)$. This term remains nearly constant throughout the period of strong illumination and then smoothly tapers toward zero as solar input declines. With this formulation, the model successfully captures both the steep initial temperature rise-dominated by the panel's thermal time constant-and the extended cooling period governed by convective and radiative heat loss to the surrounding tunnel environment. The close

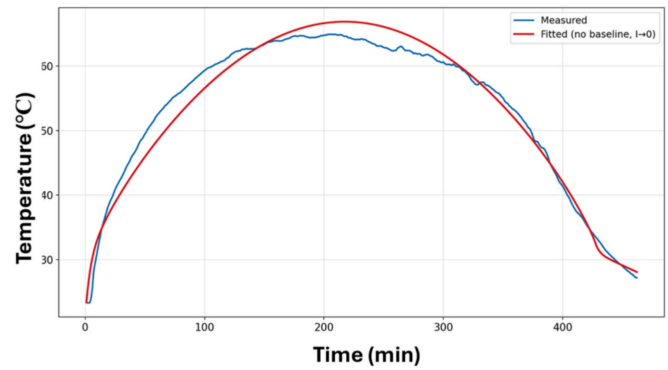

Fig. 9. Measured panel 1 temperature profile (blue) and best-fit lumped-parameter thermal model (red). The model implements the energy balance. (For interpretation of the references to colour in this figure legend, the reader is referred to the web version of this article.)

agreement between simulation and experiment (RMSE ≈ 1 °C) confirms that the simplified lumped-parameter framework captures the primary thermal physics of the PTST system and provides a robust basis for extracting key parameters such as the overall loss coefficient, effective absorptance, and the time-dependent heating-input profile.

Although the agreement between the model and experimental data is strong (RMSE ≈ 1 °C), uncertainties remain associated with the estimation of effective absorptance, heat-loss coefficients, ambient boundary conditions, and the assumed absorbed-power profile. Sensitivity analysis conducted during the fitting process indicated that moderate variations in these parameters produced only limited changes in the overall temperature evolution, suggesting reasonable robustness of the model predictions. The present lumped-parameter approach is therefore intended as a first-order representation of the dominant thermal processes governing system behavior. Future studies may incorporate formal uncertainty quantification, spatially resolved temperature distributions, and more detailed heat-transfer mechanisms to further enhance predictive capability.

$mc_p\,\frac{dT}{dt} = \alpha A I(t) - hA(T - T_{\mathrm{amb}}) + \varepsilon\sigma A\left(T^4 - T_{\mathrm{amb}}^4\right)$, using panel geometry and thermal properties from the experiment. The incident optical flux was parameterized as a raised half-cosine function active between normalized times $a = 0.00$ and $b = 0.871$, with shape exponent $p = 0.70$ and both peak and baseline absorbed components $(P_{\mathrm{max}}, P_{\mathrm{base}})$ fitted to the data. Convective coefficient h, emissivity ε, effective thermal mass multiplier γ, and ambient temperature T_{amb} were also fitted.

In the numerical model, the $Fe_3O_4@Cu_{2-x}S$ transparent photothermal panels are treated as the sole active solar-energy-conversion components. The absorbed solar radiation within each panel is calculated from the experimentally determined optical absorption characteristics and incorporated into the thermal analysis as a volumetric heat-generation term. In contrast, the solar tunnel structure, including the solar dome, reflective interior surfaces, and enclosed air space, is modeled as a passive optical and thermal environment that affects irradiance distribution, heat transfer, and thermal retention but does not generate heat directly. This distinction enables the model to separately evaluate the photothermal contribution of the transparent panels and the thermal-management role of the tunnel structure.

Photothermal conversion efficiency (PCE) Calculation

To quantify the overall performance of the photothermal solar tunnel (PTST), the system–level photothermal conversion efficiency (PCE) was calculated based on the experimentally measured surface temperatures of all six photothermal panels and the estimated incident solar irradiance on each panel. Because the tunnel operates in a radiative–-transport–dominated regime and the panels are mounted on glass substrates with negligible thermal energy storage in the nanoparticle layer, the PCE was computed using a stored–energy formulation referenced to the thermal mass of the glass panels.

The photothermal conversion efficiency (PCE) calculations used in this work follow the methodology previously established for multilayer transparent photothermal systems reported in Ref. [14]. The total thermal energy generated by the PTST was obtained by summing the heat generated from all transparent photothermal layers within the tunnel structure under solar irradiation. The overall system efficiency was then determined by comparing the accumulated thermal energy output with the incident solar energy entering the solar dome aperture. Unlike conventional solar thermal collectors based on circulating fluids, the present PCE represents direct photothermal energy generation within a transparent multilayer architectural structure designed for distributed thermal harvesting.

Using an FLIR-PV78 Solar Irradiance Meter, the light power densities (LPD) were measured at different locations: 1) outside surface of the solar dome, 2) inner surface of the solar dome, and 3) top surfaces of each photothermal panels. The light meter was positioned at multiple positions for LPD measurements and average was calculated. For outside surface of the solar dome, 13 LPD values were recorded resulting in an average of 72 mW/cm^2. On the inner surface of the solar dome, the average LPD was 66 mW/cm^2. For parallel photothermal panels (Fig. 2), the average LPD values decrease considerably from 52 mw/cm^2 on the first panel to 12 mW/cm^2 on the sixth panel. Nonetheless, as shown in Fig. 5, despite the optical power attenuation, each panel can still generate appreciable amounts of thermal energy. Due to geometric attenuation, angular mismatch, partial surface illumination, and cumulative transmission losses through the solar dome and successive photothermal panels, the effective irradiance at each stage was substantially reduced relative to the ambient solar input. Based on the measured values, the average irradiances assigned to Panels 1 through 6 were 52, 30, 25, 17, 14, 12 mW cm^{-2}, respectively. It must be noted that the light power density of 12 mW/cm^2 on the sixth panel was estimated due to damage of that panel. It must be noted that the light power density of 12 mW cm^{-2} on the sixth panel was estimated due to localized physical damage of that panel during outdoor measurements. The estimated irradiance was obtained from the experimentally observed attenuation trend across the preceding panels and the cumulative optical transmission losses within the tunnel. Because the irradiance reduction exhibited a consistent monotonic decay along the tunnel axis, the estimated value is considered a reasonable approximation for evaluating the overall photothermal performance of the multilayer PTST system.

The power conversion efficiency (PCE) of the 6-panel photothermal solar tunnel (PTST) stack was evaluated by considering the cumulative thermal energy generated by all panels over the 450-minute solar exposure period (10:00–17:30). This system-level approach captures the total energy harnessed by the full stack rather than individual panel performance.

With discrete measurements recorded at 1-minute intervals, the instantaneous thermal power of panel i is approximated as:

$$P_{\text{out},i}(t) \approx \frac{Q_i(t+\Delta t) - Q_i(t)}{\Delta t} \tag{13}$$

where $\Delta t = 60$ s and Q_i is in kJ (converted to J when computing power in watts). Explicitly:

$$P_{\text{out},i}(t) = \frac{\Delta Q_i(t) \times 1000}{60}$$

The total instantaneous output power of the stack is then:

$$P_{\text{out, total}}(t) = \sum_{i=1}^{6} P_{\text{out},i}(t) \tag{14}$$

The incident power for each panel is calculated from the measured irradiances 52, 30, 25, 17, 14, 12 mW/cm^2 and panel area A = 529 cm^2:

$$P_{\text{in, total}} = \sum_{i=1}^{6} I_i \cdot A = 79.35 \text{ W}$$

The instantaneous power conversion efficiency is:

$$_{\text{PCE}}(t) = \frac{P_{\text{out, total}}(t)}{P_{\text{in, total}}} \times 100\% \tag{15}$$

From the experimental data, the instantaneous output reaches a peak of $P_{\text{out}} \approx 50$ W, giving:

$$_{\text{PCE, peak}} \approx \frac{50}{79.35} \times 100\% \approx 63\%$$

Time-Averaged PCE

For a more representative metric over the entire exposure period, the time-averaged output power is:

$$\overline{P}_{\text{out}} = \frac{Q_{\text{total}}}{t_{\text{total}}} = \frac{1.28 \times 10^6 \text{ J}}{27,000 \text{ s}} \approx 47.4 \text{ W}$$

The corresponding average PCE of the system is:

$$\overline{\text{PCE}} = \frac{\overline{P}_{\text{out}}}{P_{\text{in, total}}} \approx \frac{47.4}{79.35} \approx 0.60 = 60\%$$

Summary

- Peak PCE: ≈ 60–65%
- Average PCE (system-level): ≈ 60%

This confirms that the PTST stack converts a substantial fraction of incident solar energy into usable thermal power, with the reported values reflecting the combined performance of all six panels. The 60% PCE of the solar tunnel is consistent with our previous experimental results from a photothermal generator [14]. In this previous study, a similar multi-panel structure was developed in a cuboid but with much smaller dimensions. This high PCE reflects the cascaded design's efficiency: upstream panels absorb high-energy photons while transmitting ~65% AVT to downstream layers, enabling spectrum-splitting across the stack. The time-resolved integration captures full energy harvest despite diurnal irradiance variations and cooling losses. Exact trapezoidal integration of the full 450 × 6 dataset yields a refined value; the 60% figure represents a conservative peak-performance estimate.

In calculating the photothermal conversion efficiency (PCE), the thermal energy contribution was attributed to the transparent Fe_3O_4@$Cu_{2-x}S$ photothermal panels, which are the designed solar-to-thermal conversion elements of the PTST system. The tunnel enclosure primarily serves as an optical guiding structure, and its inner surface was coated with a highly reflective material to minimize parasitic solar absorption. Although residual absorption and heat generation from the tunnel wall cannot be completely excluded due to non-ideal reflection and geometric effects, the quantitative separation between the heat generated by the photothermal panels and the tunnel enclosure was not experimentally determined in the present study. Such an energy partition analysis requires additional controlled experiments and will be investigated in future studies. Given the absence of photothermal absorbers in the tunnel wall and the reflective design of the enclosure, the measured thermal energy generation is considered to be predominantly associated with the Fe_3O_4@$Cu_{2-x}S$ photothermal panels.

A further implication of the present system emerges when considering operation beyond direct solar exposure. Recent work has demonstrated that plasmonic Fe_3O_4@$Cu_{2-x}S$ thin films can effectively generate heat under diffused indoor illumination, owing to their strong ultraviolet and infrared absorption mediated by localized surface plasmon resonance [34]. In a related configuration, a Diffused Light Photothermal Box (DLPB) incorporating similar transparent panels achieved internal temperatures exceeding 50–55 °C under non-direct lighting conditions, confirming that significant photothermal conversion can occur even in the absence of concentrated sunlight. This behavior suggests that the PTST concept may be extended to continuous, low-intensity heat generation driven by ambient indoor light sources, including artificial lighting. From a building system perspective, the integration of photothermal materials responsive to both direct and diffused light offers a pathway toward hybrid heating strategies, where passive solar gain during the day is augmented by indoor light-driven photothermal effects during nighttime or overcast conditions. This dual-mode functionality further reinforces the potential of plasmonic photothermal technologies as adaptable components within energy-neutral building envelopes and smart space-conditioning systems.

5. Conclusion

The Photothermal Solar Tunnel (PTST) works differently from most conventional solar heating systems. Instead of relying on a single flat collector, sunlight passes through several transparent panels arranged in a tunnel. Each panel absorbs some light, and the remaining light continues down the tunnel for direct conversion to thermal energy. In practice, this gradual absorption makes a noticeable difference compared with a single opaque surface. The panels start producing heat almost immediately. Unlike photovoltaic-based systems, which require multiple energy conversions, the PTST delivers heat as soon as sunlight hits the coatings. The $Fe_3O_4@Cu_{2-x}S$ layers absorb UV and infrared light efficiently, while most visible light passes through.

Because the panels remain visibly transparent, the interior of the tunnel stays well illuminated, a feature that could be advantageous in larger installations where daylighting is desirable. The system is lightweight and modular, enabling straightforward integration into existing structures as well as new construction. Although variations in panel spacing and orientation produced only modest changes in local temperature, the cumulative heating effect along the tunnel was consistently observed.

The photothermal energy generation mechanism of the transparent $Fe_3O_4@Cu_{2-x}S$ panels has been previously established through both individual thin-film photothermal characterization and multilayer thermal imaging experiments [14]. In the present solar tunnel architecture, the $Fe_3O_4@Cu_{2-x}S$ panels serve as the active photon-to-thermal conversion elements, while the solar tunnel functions primarily as a light-guiding and thermal-confinement structure. Accordingly, heat generation in the computational model is assigned to the photothermal panels through wavelength-selective solar absorption, whereas the tunnel walls are treated as passive optical and thermal boundaries. The objective of this study is therefore to evaluate the performance of a practical building-integrated solar tunnel system based on previously validated transparent photothermal materials and mechanisms.

Looking forward, potential improvements include developing coatings with greater spectral selectivity in the UV and IR to enhance photothermal performance, increasing thermal insulation to extend heat retention, and scaling the architecture for larger-area applications. While some operational nuances remain, the PTST concept demonstrates a practical, low-complexity approach to combining solar heating with high optical transparency. By stacking transparent, plasmonic-coated panels within a tunnel geometry, the system delivers reliable thermal gain while still transmitting substantial visible light, all without requiring heavy or intrusive infrastructure.

While our previous study established the feasibility of multilayer transparent photothermal solar harvesting using a laboratory-scale enclosure [10], the present work advances the concept toward a practical building-integrated technology by employing a commercial solar dome and cylindrical solar tunnel architecture containing multiple transparent photothermal panels. Beyond experimental validation, this study provides detailed analysis of the underlying photon-to-thermal energy conversion mechanisms associated with plasmonic $Fe_3O_4@Cu_{2-x}S$ core–shell nanoparticles, including plasmon hybridization and mode-splitting effects, as well as numerical thermal simulations of the complete solar tunnel system. These advances extend the original proof-of-concept into a more realistic and scientifically comprehensive framework for building utility heating applications.

Author contributions

Donglu Shi conceived the research concept, secured the funding, designed the study, supervised the project, developed the thermal modeling and photothermal conversion efficiency analysis, interpreted the results, and prepared the manuscript. Meher Saketh Gandharapu synthesized the photothermal nanomaterials, fabricated the transparent photothermal panels, performed optical and thermal characterization, and contributed to data analysis. Anudeep Katepalli conducted the outdoor photothermal solar tunnel experiments, collected experimental data, and contributed to data processing and interpretation. Anton Harfmann secured the research funding and contributed to the design, fabrication, and assembly of the photothermal solar tunnel system and developed the architectural designs for retrofit solar tunnel applications. Mathias Bonmarin contributed to the engineering design, construction, and implementation of the solar tunnel system and participated in technical discussions related to system development. John Krupczak contributed to the conceptual development of the building utility heating applications, heat transfer studies and modeling, and critical revision of the manuscript. All authors reviewed, revised, and approved the final manuscript.

Abbreviations	
PTST	Photothermal Solar Tunnel
PT	Photothermal
PTP	Photothermal Panels
AVT	Average Visible Transmittance
LSPR	Localized Surface Plasmon Resonance
PE	Polyethylene
DLPB	Diffused Light Photothermal Box
Optical, Electronic, and Radiative Parameters	
Geometric & Wave Parameters	
a	Radius of nanoparticle
λ	Wavelength of incident light
k	Wavevector magnitude ($k = 2\pi/\lambda$)
$\mathbf{q}$	Momentum (wavevector in dielectric response)
Dielectric & Material Response	
$\varepsilon(\omega)$	Complex dielectric function of particle
ε_m	Dielectric constant of surrounding medium
ε_∞	High-frequency dielectric constant
$\varepsilon_2(\omega) = \mathrm{Im}[\varepsilon(\omega)]$	Loss (imaginary dielectric part)
$\mathrm{Re}[\varepsilon(\omega)]$	Real part of dielectric function
Electronic & Many-Body Response	
$\Pi(\mathbf{q},\omega)$	Polarization (density–density response function)
$\varepsilon(\mathbf{q},\omega)$	Nonlocal dielectric function
e	Electron charge
ε_0	Vacuum permittivity
Drude/Optical Model Parameters	
ω	Angular frequency of incident field
ω_p	Plasma frequency
γ	Electron damping rate (bulk)
$\Delta\varepsilon_{\mathrm{inter}}(\omega)$	Interband correction
Polarizability & Scattering	
$\alpha(\omega)$	Quasi-static polarizability
$\alpha_{\mathrm{eff}}(\omega)$	Effective (dynamic/radiative corrected) polarizability
$\mathrm{Im}(\alpha)$	Imaginary part of polarizability
Optical Cross Sections & Power	
σ_{abs}	Absorption cross-section
P_{abs}	Absorbed power
Field Quantities	
$\mathbf{E}_0$	Incident electric field
$\mathbf{E}_{\mathrm{loc}}$	Local electric field at nanoparticle
$\lvert\mathbf{E}_{\mathrm{loc}}\rvert^2/\lvert\mathbf{E}_0\rvert^2$	Field enhancement factor
Resonance & Coupling Parameters	

(*continued on next page*)

(*continued*)

ω_s	Surface plasmon resonance frequency
ω_r	Resonant frequency (generalized)
$\omega_\pm$	Hybridized mode frequencies
Q	Quality factor
γ_{eff}	Effective damping rate
Hybridization/Interaction Parameters	
η	Coupling strength parameter
β	Interaction/retardation correction parameter
Radiation & Damping Corrections	
k^3term	Radiative damping contribution
k^2/aterm	Dynamic depolarization
Illumination Parameters	
I	Incident solar intensity
I_i	Incident irradiance on panel i
$I_i(t)$	Time-dependent irradiance
Thermal and Energy-Balance Parameters	
$m_i c_{p,i}$	Effective thermal mass of panel i
α_i	Spectral absorptance of panel i
A_i	Illuminated area of panel i
A	Panel area
h_i	Convective heat-transfer coefficient
ε_i	Effective emissivity of panel i
$T_{amp\beta}(t)$	Ambient air temperature
Q	Thermal energy
$Q_i(t)$	Cumulative thermal energy of panel i
$\Delta Q_i(t)$	Incremental thermal energy change of panel i
Total	Total thermal energy generated by all panels
ΔT	Temperature difference
m	Mass of sample (thin film + substrate)
C_p	Specific heat capacity of substrate
P_{heat}	Heat generation power
$P_{out,i}(t)$	Instantaneous thermal output power of panel i
$P_{out,total}(t)$	Total instantaneous output power of the PTST stack
P_{out}	Time-averaged output power
$P_{in,total}$	Total incident solar power on all panels
t_{total}	Total solar exposure duration
Performance Metrics	
PCE(t)	Instantaneous power conversion efficiency
PCE_{peak}	Peak power conversion efficiency
P¯CE	Time-averaged power conversion efficiency
Physical Constants	
σ	Stefan–Boltzmann constant

CRediT authorship contribution statement

Meher Saketh Gandharapu: Methodology, Data curation. **Anudeep Katepalli:** Data curation. **Anton Harfmann:** Funding acquisition. **Mathias Bonmarin:** Formal analysis. **John Krupczak:** Formal analysis. **Donglu Shi:** Writing – review & editing, Writing – original draft, Visualization, Validation, Supervision, Software, Resources, Project administration, Methodology, Investigation, Funding acquisition, Formal analysis, Conceptualization.

Declaration of competing interest

The authors declare that they have no known competing financial interests or personal relationships that could have appeared to influence the work reported in this paper.

Acknowledgements

We acknowledge the financial support from National Science Foundation CMMI-1953009 and the Michelman Green, Clean and Sustainable Technology Research Innovation Program (F103484). We also acknowledge the financial support from Swiss National Science Foundation with project number: IZSEZ0_223270, titled "Photo-thermal coating for energy efficient windows."

Data availability

Data is available in a publicly accessible repository.

References

[1] M.S. Dresselhaus, I.L. Thomas, Alternative energy technologies, Nature 414 (2001) 332–337.
[2] M. Graetzel, Solar energy conversion by dye-sensitized photovoltaic cells, Inor. Chem. 44 (2005) 6842–6851.
[3] R.H. Bube, Photovoltaic materials, Imperial College Press, London, UK, 1998.
[4] V. Weitbrecht, D. Lehmann, A. Richter, Flow distribution in solar collectors with laminar flow conditions, Sol. Energy 73 (2002) 433–441.
[5] R. Fu, D. Feldman, R. Margolis, M. Woodhouse, K. Ardani, Solar Photovoltaic System Cost Benchmark: Q1 2017, United States. U.S. Department of Energy Office of Scientific and Technical Information, 2017.
[6] I. Nath, Cleaning up after clean energy: hazardous waste in the solar industry, Stanford J. Int. Relat. 11 (2010) 6–15.
[7] Phillip Irace, Harold Brandon, Solar heating in commercial buildings, in: Mechanical Engineering and Materials Science Independent Study, 2017, p. 50, https://openscholarship.wustl.edu/mems500/50.
[8] A. Jamar, Z.A.A. Majid, W.H. Azmi, M. Norhafana, A.A. Razak, A review of water heating system for solar energy applications, Int. Commun. Heat and Mass Transfer 76 (2016) 178–187, https://doi.org/10.1016/j.icheatmasstransfer.2016.05.028. ISSN 0735-1933.
[9] Muhammad Imran Khan, Faisal Asfand, Sami G. Al-Ghamdi, Progress in research and technological advancements of thermal energy storage systems for concentrated solar power, J. Energy Storage 55 (Part D) (2022), https://doi.org/10.1016/j.est.2022.105860. ISSN 2352-152X.
[10] Anudeep Katepalli, Yuxin Wang, Jou Lin, Anton Harfmann, Mathias Bonmarin, John Krupczak, Donglu Shi, A photothermal solar tunnel via multiple transparent $Fe_3O_4@Cu_{2-x}S$ thin films for heating utility application, Solar Energy 271 (2024), https://doi.org/10.1016/j.solener.2024.112444. ISSN 0038-092X.
[11] M. Lyu, J. Lin, J. Krupczak, D. Shi, Optical thermal insulation via the photothermal effects of Fe3O4 and $Fe_3O_4@Cu_{2-x}S$ thin films for energy-efficient single-pane windows, MRS Commun. 10 (3) (2020) 439–448.
[12] L. Lin, M. Lyu, D. Shi, 3D solar harvesting and energy generation via multilayers of transparent porphyrin and iron oxide thin films, Energies 16 (2023) 3173, https://doi.org/10.3390/en16073173.
[13] M. Lyu, J. Lin, L. Krupczak, D. Shi, Light angle dependence of photothermal properties in oxide and porphyrin thin films for energy-efficient window applications, MRS Commun. 10 (3) (2020) 439–448, https://doi.org/10.1557/mrc.2020.39.
[14] M. Lyu, J. Lin, J. Krupczak, D. Shi, Solar harvesting through multilayer spectral selective iron oxide and porphyrin transparent thin films for photothermal energy generation, Adv. Sustain. Syst. (2021), https://doi.org/10.1002/adsu.202100006.
[15] J. Lin, J. Krupczak, D. Shi, Solar harvesting and energy generating building skins with photothermal-photovoltaic dual modality based on porphyrin thin films, MRS Commun. (2022), https://doi.org/10.1557/s43579-022-00299-x.
[16] J. Lin, Y. Wang, M. Lyu, D. Shi, Transparent porphyrin-based hybrid films for spectral selective solar harvesting and energy generation, Sol. Energy Mater. Sol. Cells 243 (2022) 15.
[17] X. Han, Z. Deng, Z. Yang, Y. Wang, H. Zhu, B. Chen, Z. Cui, R.C. Ewing, D. Shi, Biomarkerless targeting and photothermal cancer cell killing by surface-electrically-charged superparamagnetic Fe3O4 composite nanoparticles, Nanoscale 9 (2017) 1457–1465.
[18] M.E. Donglu Shi, A.W. Sadat, Dunn, David B. Mast, Photo-fluorescent and magnetic properties of iron oxide nanoparticles for biomedical applications, Nanoscale 7 (18) (2015) 8209–8232.
[19] A. Dunn, S.M. Ehsan, D. Mast, G.M. Pauletti, H. Xu, J. Zhang, R.C. Ewing, D. Shi, Photothermal effects and toxicity of Fe3O4 nanoparticles via near infrared laser irradiation for cancer therapy, Mater. Sci. Eng. C 46 (2015) 97–102.
[20] Y. Zhao, M.E. Sadat, A.W. Dunn, H. Xu, C.-H. Chen, W. Nakasuga, R.C. Ewing, D. Shi, Photothermal effect on Fe3O4 nanoparticles irradiated by white-light for energy-efficient window applications, Solar Energy Mater Solar Cells. 161 (2017) 247–254.
[21] Y. Zhao, A. Dunn, J. Lin, D. Shi, Photothermal effect of nanomaterials for efficient energy applications, in: Novel Nanomaterials for Biomedical, Environmental and Energy Applications, Elsevier, 2019, pp. 415–434.
[22] M.E. Sadat, M.K. Baghbador, A.W. Dunn, H.P. Wagner, R.C. Ewing, J. Zhang, Xu. Hong, G.M. Pauletti, D.B. Mast, D. Shi, Photoluminescence and photothermal effect of Fe3O4 nanoparticles for medical imaging and therapy, Appl. Phys. Lett. 105 (9) (2014) 091903.
[23] M. Lyu, J. Lin, D. Shi, Solar desalination via multilayers of transparent photothermal $Fe_3O_4@Cu_{2-x}S$ thin films, Energ. Technol. 2100590 (2021), https://doi.org/10.1002/ente.202100590.
[24] Q. Tian, J. Hu, Y. Zhu, R. Zou, Z. Chen, S. Yang, R. Li, Q. Su, Y. Han, X. Liu, Sub-10 nm $Fe_3O_4@Cu_{2-x}S$ core-shell nanoparticles for dual-modal imaging and photothermal therapy, J. Am. Chem. Soc. 135 (23) (2013) 8571–8577.
[25] J. Lin, D. Shi, Photothermal and photovoltaic properties of transparent thin films of porphyrin compounds for energy applications, Appl. Phys. Rev. 8 (2021) 011302, https://doi.org/10.1063/5.0036961.
[26] R. Cornell, U. Schwertmann, The Iron Oxides: Structure, Properties, Reactions, Occurrences and Uses, 2nd ed., Wiley-VCH, 2003, 10.1002/3527602097.

[27] W. van der Stam, S. Gudjonsdottir, W.H. Evers, A.J. Houtepen, Switching between plasmonic and fluorescent copper sulfide nanocrystals, J. Am. Chem. Soc. 139 (37) (2017) 13208–13217, https://doi.org/10.1021/jacs.7b07788. Epub 2017 Sep 7. PMID: 28841295; PMCID: PMC5609121.
[28] E. Prodan, C. Radloff, N.J. Halas, P.A. Nordlander, Hybridization model for the plasmon response of complex nanostructures, Science 302 (5644) (2003) 419–422, https://doi.org/10.1126/science.1089171.
[29] S.A. Maier, Plasmonics: Fundamentals and Applications, Springer, 2007, 10.1007/0-387-37825-1.
[30] G.D. Mahan, Many-Particle Physics, 3rd ed., Springer, New York, 2000, 10.1007/978-1-4757-5714-9.
[31] L. Zhou, Y. Tan, J. Wang, et al., Self-assembly of highly efficient, broadband plasmonic absorbers for solar steam generation, Science 345 (2014) 546–550.
[32] H. Ghasemi, G. Ni, A.M. Marconnet, et al., Solar steam generation by heat localization, Nat. Commun. 5 (2014) 4449.
[33] Z. Liu, H. Song, D. Ji, et al., Extremely cost-effective and efficient solar vapor generation under nonconcentrated illumination using thermally isolated black paper, Global Chall. 1 (2017) 1600003.
[34] A. Katepalli, N.K. Tene, Y. Wang, A. Harfmann, M. Bonmarin, J. Krupczak, D. Shi, Photothermal Utility heating with diffused indoor light via multiple transparent Fe3O4@Cu2−xS thin films, Energy Technol. 12 (2024) 2400703, https://doi.org/10.1002/ente.202400703.